crystals

MDPI

Article

Effect of Sn Addition on the Microstructure and Age-Hardening Response of a Zn-4Cu Alloy

Aysha E. Shamaki, Heba Y. Zahran and Alaa F. Abd El-Rehim *

Physics Department, Faculty of Science, King Khalid University, P.O. Box 9004, Abha 61413, Saudi Arabia; ayo88osh@gmail.com (A.E.S.); heldemardash@kku.edu.sa (H.Y.Z.)
* Correspondence: alaa.abdelrehim@kku.edu.sa

Abstract: The aim of this research is to assess the influence of Sn inclusion on the microstructure evolution and age-hardening response of a Zn-4Cu alloy. This is the first study to correlate the age-hardening response to the microstructure of Zn-4Cu alloy reinforced with different Sn contents. A series of Zn-4Cu-Sn alloys were successfully fabricated with different Sn concentrations in the range of 0.0–4.0 wt.% using permanent mold casting. The microstructure of Zn-4Cu-Sn alloys was investigated by means of a scanning electron microscope (SEM) attached with an energy dispersive spectroscope (EDS) and X-ray diffraction (XRD) line profile analysis. At room temperature, the Vickers microhardness measurements were used to assess the age-hardening response of alloys. The results show that the microhardness of the Zn-4Cu (ZC) binary alloy increases a little bit from 76 to 80 HV as the aging time increases from 2 to 128 h, respectively. For aging times up to 16 h, the microhardness of all Sn-containing alloys decreases but then increases again. The lowest hardness belongs to the ZC-1.5Sn alloy, and the Sn-Zn-3.0Sn alloy has the highest; the other alloys fall somewhere in between. At high aging times (64 and 128 h), the microhardness of all Sn-containing samples increased continuously with an increasing Sn content from 0.0 to 3.0 wt.%. When the Sn-containing alloys (3.5 and 4.0 wt.% Sn) were aged for 64 and 128 h, the hardness declined by 7.94% and 8.90% compared to their peak aging hardness values, respectively. By considering the structural changes that occur in the Zn-4Cu-Sn alloys, the reasons for the observed variations in microhardness data with increasing Sn content and aging time were elucidated. X-ray diffraction (XRD) data was analyzed to determine the zinc matrix's lattice parameters, c/a ratio, and unit cell volume variations.

Keywords: Zn-Cu based alloys; Sn content; aging; microhardness; microstructure

check for updates

Citation: Shamaki, A.E.; Zahran, H.Y.; Abd El-Rehim, A.F. Effect of Sn Addition on the Microstructure and Age-Hardening Response of a Zn-4Cu Alloy. *Crystals* **2023**, *13*, 1635. https://doi.org/10.3390/cryst13121635

Academic Editors: Andrey Prokofiev, Weijun He, Zejun Chen, Meini Yuan and Baoxi Liu

Received: 11 September 2023
Revised: 13 October 2023
Accepted: 20 November 2023
Published: 25 November 2023

Copyright: © 2023 by the authors. Licensee MDPI, Basel, Switzerland. This article is an open access article distributed under the terms and conditions of the Creative Commons Attribution (CC BY) license (https://creativecommons.org/licenses/by/4.0/).

1. Introduction

Zinc (Zn) has promising potential applications in biodegradable bone implants due to its moderate degradation rate and biological safety in the human body [1]. Zn belongs to the essential trace elements in human nutrition and plays a significant role in multiple biochemical functions, such as wound healing, cell growth, and cell division [2,3]. Therefore, Zn might be a viable candidate for biodegradable material. However, there are some drawbacks of pure Zn, such as its poor strength and ductility, which fail to meet the mechanical property requirements for medical metal implants [4,5].

Alloying is a popular technique to enhancing the mechanical characteristics of pure Zn. Various amounts of alloying elements were used to improve the mechanical properties of Zn alloys such as Mg [6], Fe [7], Ag [8], Ca [9], Mn [10], Cu [11], Ti [12], Li [13], and rare earth elements (REEs) [14]. Copper (Cu) is one of the essential trace elements for humans, with a normal level of 1.1–1.5 μg/mL found in blood serum, making it a superior alloying element [15]. Additionally, Cu improves antibacterial properties for clinical applications, which can reduce the infection risk [16]. Zn-Cu alloys exhibited significant antibacterial effects and acceptable cytotoxicity to human endothelial cells [17]. The Zn-Cu alloy exhibited excellent strength and ductility, uniform and slow degradation, good

biocompatibility, and significant antibacterial effect, which made it an excellent candidate material for biodegradable implants, especially for cardiovascular stents application. Moreover, the Zn-Cu alloys have demonstrated potential as absorbable materials for applications in orthopedic implants and cardiovascular stents, principally due to their desirable corrosion behavior.

The mechanical features and microstructure evolutions of Zn-Cu-based alloys have been explored and reported in several studies under different test conditions. Mostaed et al. [18] deduced the effect of precipitates and grain size variations on the mechanical features of Zn-1wt.% Cu alloy. The cold rolling of a Zn-1Cu alloy produced ε-$CuZn_5$ precipitates at an ultrafine-grained structure. At a 1.0×10^{-4} s^{-1} strain rate, the Zn-1Cu alloy exhibited a maximum elongation of 470%. Huang et al. [19] explored the influence of Cu concentration (1, 2, and 3 wt.%) on the mechanical features and microstructure development of Zn-Cu alloys. The authors found that the ε-$CuZn_5$ second phase and the primary α-Zn matrix affected the mechanical characteristics of the investigated alloys. With a copper content increment, the microhardness augmented from 34.3 to 76.64 Hv and the strength increased from 6.68 to 105.5 MPa, while the elongation declined from 8.17 to 1.70%, then increased to 4.06%. Yue et al. [20] reported that a large volume fraction of ε-$CuZn_5$ intermetallic compounds (IMCs) within the primary α-Zn matrix could be detected in the as-cast Zn-3Cu alloy, even after homogenized heat treatment. Tang et al. [21] examined the microstructure development of Zn-xCu alloy samples with various Cu contents (x = 1, 2, 3, and 4 wt.%). They found that the volume fraction of the $CuZn_5$ phase increased as the concentration of Cu increased. Niu et al. [22] investigated the impact of hot extrusion on the mechanical features and microstructure evolutions of the Zn-4Cu alloy. They concluded that the $CuZn_5$ precipitates were distributed along the extrusion direction due to hot extrusion.

However, some research papers have reported that the Zn-Cu alloys exhibited poor strength and softening behavior during processing [23,24]. They are primarily plagued by a performance decline above 80–90 °C and/or after long natural aging at room temperature [25,26]. Therefore, inadequate mechanical characteristics are still a serious concern that confines the application of Zn-Cu alloys. It is widely acknowledged that the addition of a second reinforcing element is a powerful method to promote the mechanical features of Zn-Cu alloys due to the microstructure modifications. Liu et al. [27] explored the implications of 0.5 wt.% Mg addition on the mechanical behavior of Zn-1Cu and Zn-3Cu alloys during multi-pass equal channel angular pressing (ECAP). After ECAP, both Zn-Cu-Mg alloys showed significant tensile strength and ductility increases. In another related research study, Tang et al. [16] concluded that the 1 wt.% Mg additive to binary Zn–3Cu considerably enhanced its mechanical properties due to the development of Mg_2Zn_{11} IMC and the effective refinement of the microstructure. Furthermore, the observed increment of the tensile yield strength (σ_{TYS}) and ultimate tensile strength (σ_{UTS}) is from 214 to 250 MPa and 427 to 440 MPa, respectively. The effect of (0.5 and 1.0 wt.%) iron additives on the Zn–3Cu alloy has been investigated [20]. The microstructure of Zn-3Cu-0.5Fe and Zn–3Cu-1.0Fe alloys consisting of $FeZn_{13}$ phase, ε-$CuZn_5$ precipitates, and α-Zn matrix. With a higher iron content, both the σ_{TYS} and σ_{UTS} increased. Zhang et al. [28] fabricated Zn-2Cu alloy with 0.05 and 0.1Ti. They found that the microstructure consisted of $TiZn_{16}$ and $CuZn_5$ IMCs, which were evenly dispersed throughout the α-Zn matrix. The Zn-2Cu-0.05Ti alloy showed optimal mechanical characteristics. The ultimate tensile strength and elongation of the 0.05Ti-containing alloy increased by 38.7% and 19.1%, respectively, compared with the binary alloy.

In summary, the mechanical properties of Zn-Cu alloys can be enhanced by tailoring their microstructures via alloying and special fabrication techniques followed by several post treatment. Zn-Cu based biodegradable alloys have the potential to be developed to next-generation orthopedic implants as alternatives to conventional implants to avoid revision surgeries and to reduce biocompatibility issues. They can be used for a variety of biomedical applications, such as wound closure devices (biodegradable staples, surgical tacks, plugs, microclips, and rivets), orthopedic fixation devices (fixative plates, screws,

and porous scaffolds), cardiovascular stents, and bone implants. Sufficient mechanical properties are the key prerequisites for Zn-Cu based alloys to be qualified as biodegradable metallic materials. It is crucial to develop Zn-Cu based alloys without a clear and thorough understanding of their microstructural and mechanical properties and without adequate reliability data. To the best of our knowledge, no previous research has examined the impact of Sn inclusion and aging duration on the microstructure and age-hardening response of the Zn-4Cu alloy. The lack of such an investigation motivated the present work. This is the prime novelty of the present work.

2. Materials and Methods

2.1. Materials

The binary Zn-4 wt.% Cu alloy and ternary alloys of Zn-4 wt.% Cu-x wt.% Sn (where x = 0, 0.5, 1.0, 1.5, 2.0, 2.5, 3.0, 3.5, and 4.0 wt.%) were fabricated using pure Zn (99.99%), pure Cu (99.98%), and pure Sn (99.96%). To avoid oxidation, the raw materials were melted with the protection of argon atmosphere at 550 °C in an electrical resistance furnace for 30 min using high-graphite crucibles. The molten alloys were stirred for 20 s before being chill cast into a cylinder-shaped mild steel mold at room temperature (25 °C). The cast alloys were sliced into 5 mm × 5 mm × 2 mm block samples for metallographic characterization and microhardness testing. Table 1 displays the results of an inductively coupled plasma emission spectrometer (ICP-AES) analysis of the alloys' chemical compositions. The chemical composition of the as-cast alloys is very close to their nominal compositions. The solution heat treatment (SHT) of specimens was performed for 24 h at 350 °C, followed by iced water quenching at 0 °C. After the SHT, the samples were aged at 100 °C for different times (0, 2, 4, 8, 16, 32, 64, and 128 h), followed by iced water quenching at 0 °C to cease further aging reactions. Figure 1 displays a graphical representation of the heat treatment process. The temperature measurement accuracy was ±1 °C.

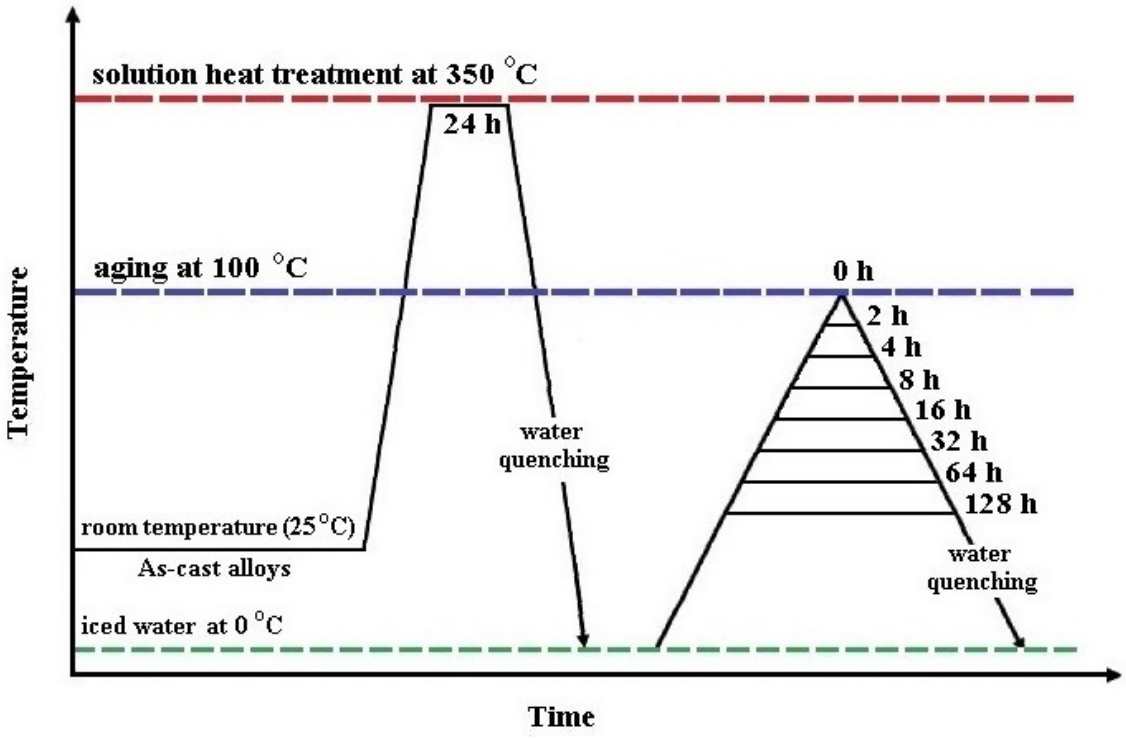


Figure 1. A schematic diagram showing the heat treatment procedure.

Table 1. Chemical composition of the experimental Zn-4Cu-xSn alloys analyzed by inductively coupled plasma atomic emission spectroscopy (ICP-AES).

Alloy	Notation	Element Content (wt.%)		
		Cu	Sn	Zn
Zn-4Cu	ZC	4.1	0	Bal.
Zn-4Cu-0.5Sn	ZC-0.5Sn	3.98	0.48	Bal.
Zn-4Cu-1.0Sn	ZC-1.0Sn	3.96	0.96	Bal.
Zn-4Cu-1.5Sn	ZC-1.5Sn	3.95	1.47	Bal.
Zn-4Cu-2.0Sn	ZC-2.0Sn	3.92	1.95	Bal.
Zn-4Cu-2.5Sn	ZC-2.5Sn	3.94	2.48	Bal.
Zn-4Cu-3.0Sn	ZC-3.0Sn	3.92	2.91	Bal.
Zn-4Cu-3.5Sn	ZC-3.5Sn	3.91	3.44	Bal.
Zn-4Cu-4.0Sn	ZC-4.0Sn	3.88	3.93	Bal.

2.2. Microstructure Characterization

To characterize the microstructure, the samples were first ground with various grades of polishing paper before being polished with 0.25 mm diamond paste. After etching for 1–5 s in a solution of 3 mL HNO_3, 2 mL HCl, and 95 C_2H_5OH, the microstructure was analyzed by revealing grain boundaries. After that, anhydrous ethyl alcohol was used to clean the samples and then dried them in a blast of air. The drying step produces the visual contrast between grains, not the etching process. The morphology and elemental composition of the current alloys were characterized using a JEOL JSM-6480LV scanning electron microscope (SEM) attached to an energy dispersive spectroscope (EDS) analyzer operating at an accelerating voltage of 20 kV. An X-ray diffractometer (XRD) (Model Shimadzu D6000 with Ni-filtered CuK_α radiation (λ = 1.5406 Å)) operated at 30 kV and 30 mA was employed to perceive the phase constitutions of the prepared alloys. The XRD spectra were collected over a 2θ range of 20°–80° at a scan rate of 2° per minute and a step size of 0.02°.

2.3. Microhardness Tests

Vickers microhardness measurements were performed on a Vickers Microhardness Tester (MH3, Metkon, Bursa, Turkey) with an applied load of 300 g and a dwell time of 15 s. In order to ensure reproducibility, each reported hardness value was calculated by taking the average of 10 random measurements.

3. Results and Discussion

Figure 2 exhibits a representative SEM image of the as-cast Zn-4Cu alloy before thermal aging. The microstructure of the Zn-4Cu alloy consists of a primary α-Zn matrix and a secondary ε-$CuZn_5$ phase. The ε-$CuZn_5$ phase has an irregular and polygon-like morphology. Figure 2 displays the energy dispersive spectroscope (EDS) analysis results for the chemical composition of each phase. The EDS qualitative analysis confirmed that the alloy mainly consisted of α-Zn and CuZn5 phases, whose morphology is in agreement with previous studies about the Zn-Cu binary alloy [29,30]. This is in line with the earlier work of Tang et al. [21], who studied the microstructure of the as-cast Zn-*x*Cu alloys (*x* = 1, 2, 3, and 4 wt.%). They found that the microstructure of the as-cast alloys consisted of a second phase of $CuZn_5$ within the primary α-Zn matrix. According to the binary phase diagram of the Zn-Cu system [31,32], the peritectic reaction is described by Zn + L → ε-$CuZn_5$ and takes place at 425 °C. The $CuZn_5$ phase develops in a nonaligned way. As a result, when the temperature decreases to around 425 °C during solidification, the ε-$CuZn_5$ phase precipitates from the melt first. At 425 °C, a temperature greater than the melting point of pure Zn (419.6 °C), the ε-$CuZn_5$ phase is stable, as reported by Kattner and Massalski [33]. Consequently, the ε-$CuZn_5$ phase cannot be dissolved into the Zn matrix after solution treatment at 350 °C. Figure 3 shows representative microstructures of the as-cast Sn-containing alloys. It is clearly seen that after adding the Sn element to the

Zn-4Cu alloy, no new phases were formed in the primary α-Zn matrix, indicating that most of Sn was dissolved in the matrix. There was no significant change in the volume fraction of the ε-$CuZn_5$ phase with an increasing Sn content. Consequently, it is expected that there will be no corresponding change in hardness values with an increasing Sn concentration.

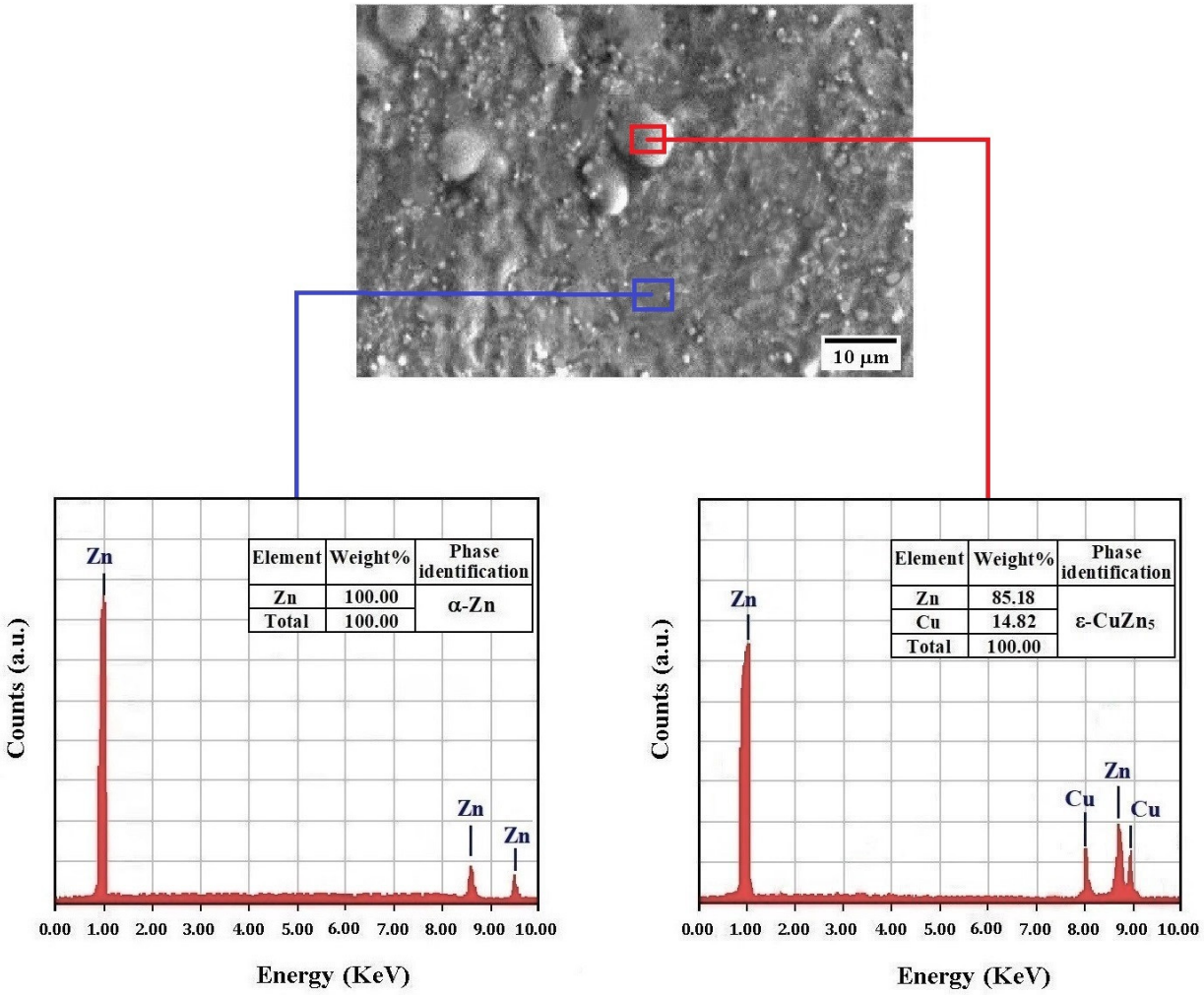


Figure 2. Representative SEM micrograph and the corresponding EDS spectra of the as-cast Zn-4Cu alloy.

The age-hardening response is depicted in Figure 4 for Zn-4Cu-xSn (x = 0, 0.5, 1.0, 1.5, 2.0, 2.5, 3.0, 3.5, and 4.0 wt.%) alloys aged at 100 °C for different times (0, 2, 4, 8, 16, 32, 64, and 128 h). The markers represent experimental points, and the dashed lines interpolate between them. It should be mentioned that the solution heat treatment (aging time = 0) of all present alloys does not produce a significant change in the age-hardening response. Consequently, the data on solution heat treatment was excluded from the current study. The microhardness of the Zn-4Cu (ZC) binary alloy increased a little bit from 76 to 80 HV with the aging time increment from 2 to 128 h, respectively. For Sn-containing alloys, alloys range in hardness from the softest (ZC-1.5Sn) to the hardest (ZC-3Sn). For aging times up to 16 h, microhardness in all Sn-containing alloys decreases but then increases again.

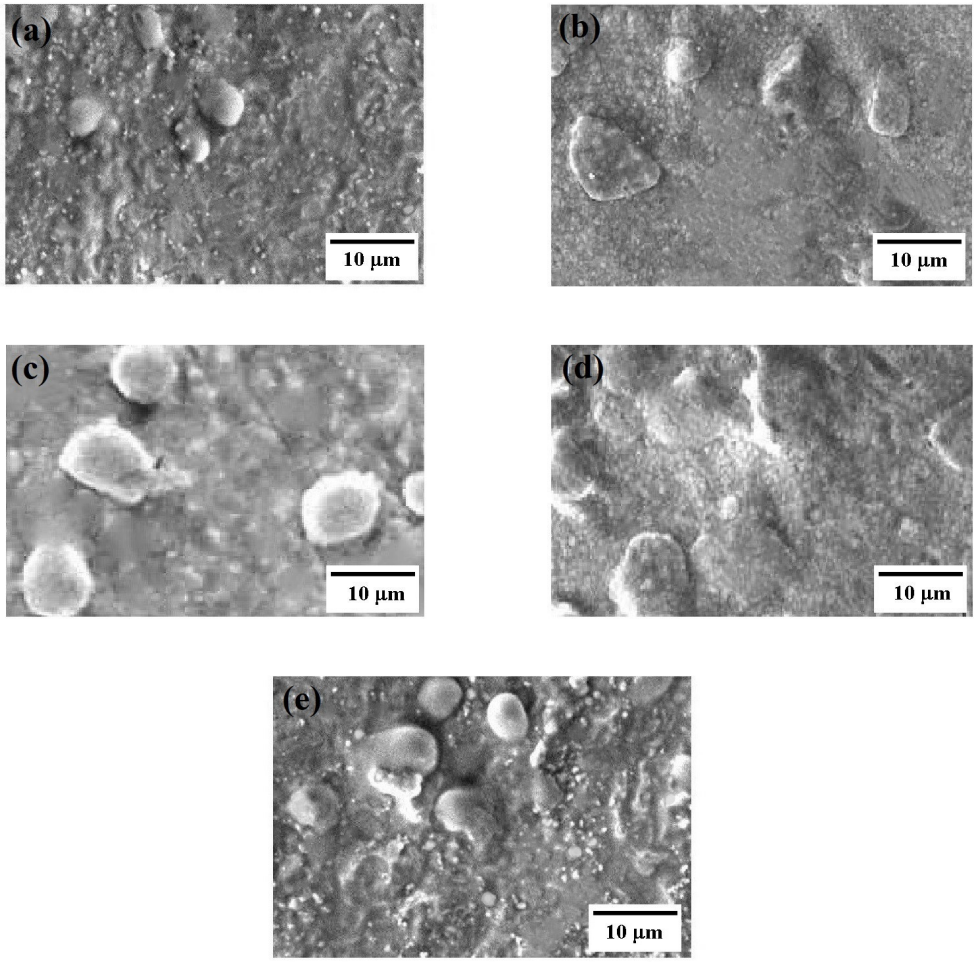


Figure 3. Representative SEM micrographs of the as-cast (**a**) Zn-4Cu alloy, (**b**) Zn-4Cu-1.0Sn alloy, (**c**) Zn-4Cu-2.0Sn alloy, (**d**) Zn-4Cu-3.0Sn alloy, and (**e**) Zn-4Cu-4.0Sn alloy.

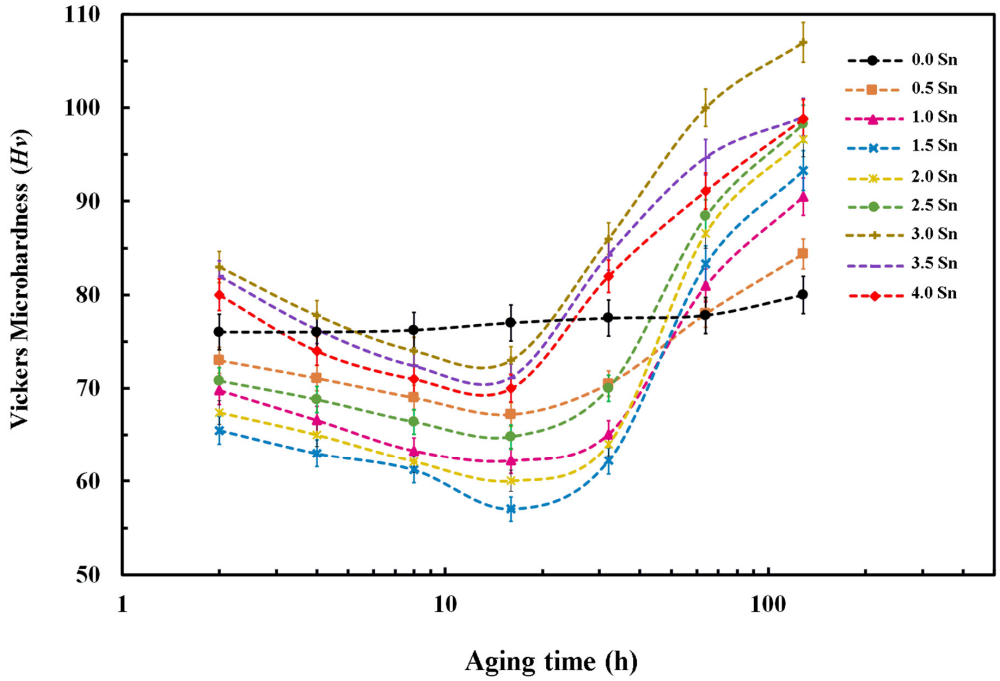


Figure 4. Age-hardening curves at 100 °C for Zn-4Cu-Sn alloys with various Sn contents.

Typical microstructures of ZC specimens aged at 100 °C for 2 and 128 h are represented in Figure 5a,b, respectively. Microstructure evolution revealed the presence of primary α-Zn as a matrix and dark secondary phase. The volume fraction of the dark secondary phase increases with the variation of aging time from 2 to 128 h. The dark secondary precipitates were identified as the ε-$CuZn_5$ phase. The ε-$CuZn_5$ phase has an irregular and polygon-like morphology. The results of the quantitative analysis with EDS estimated the composition of each phase. Figure 5c and d shows the EDS qualitative analysis of the primary α-Zn phase and the ε-$CuZn_5$ phase, which reveal that the α-Zn is the main constituent (98.69 wt.%), while the ε-$CuZn_5$ phase is composed of about 84.26 wt.% Zn and 15.74 wt.% Cu. The microstructure is quite similar to that observed by Lin et al. [29] and Wang et al. [30]. The variation of aging time from 2h to 128 h leads to the increment of the ε-$CuZn_5$ precipitate's volume fraction (Figure 5b). As a result, the microhardness would increase by a small amount.

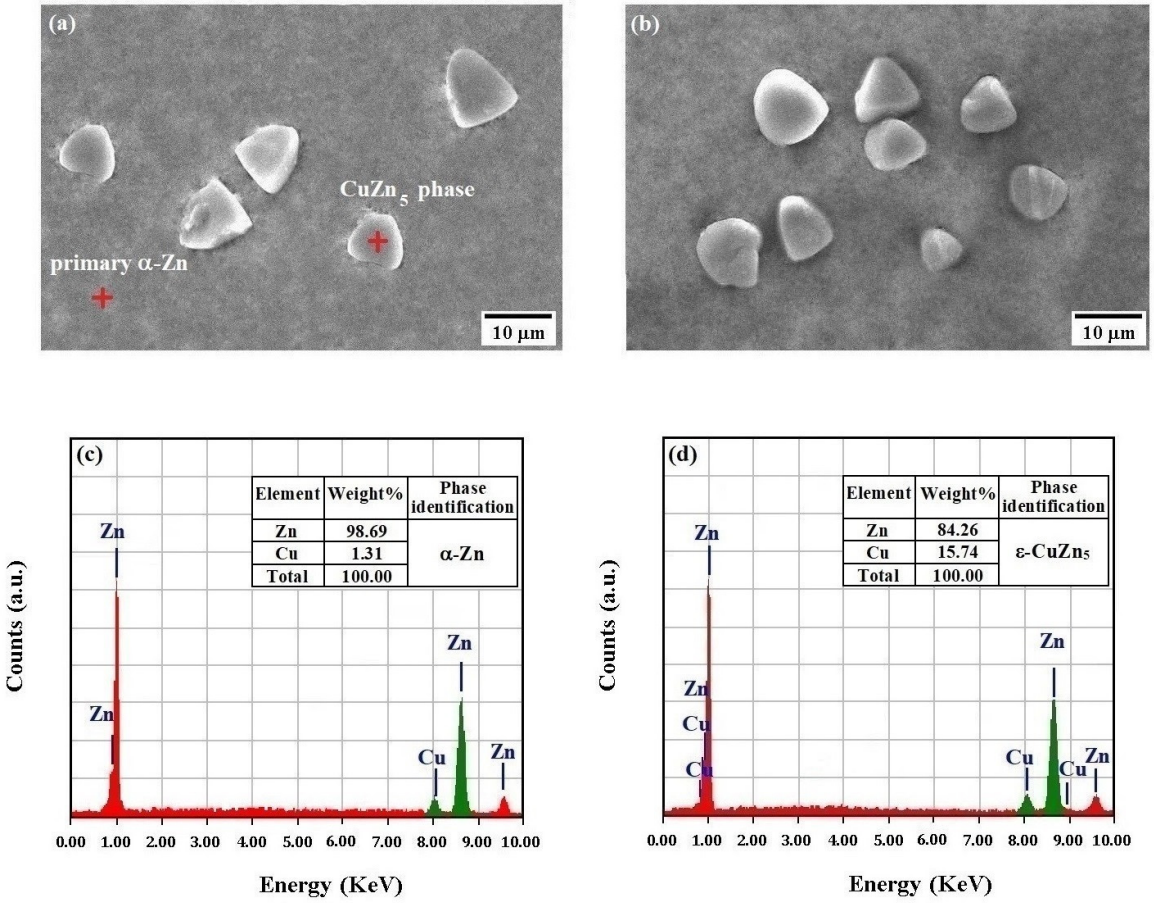


Figure 5. Representative SEM micrographs of ZC alloy aged at 100 °C for (**a**) 2 h and (**b**) 128 h (**c**) EDS results of α-Zn phase and (**d**) EDS results of ε-$CuZn_5$ phase.

An alternative graphical representation of the age-hardening curves is shown in Figure 6 to clarify the effect of Sn addition on the microhardness of Zn-4Cu alloy. The microhardness values of all Sn-containing alloys are reduced with Sn concentrations up to 1.5 wt.% for shorter aging durations (2 to 32 h). When the Sn content is increased from 1.5 to 3.0 wt.%, the hardness increases considerably. For all shorter aging times, the ZC alloy containing 3.0 wt.% Sn achieves the peak microhardness (i.e., the ZC alloy containing 3.0 wt.% Sn exhibits the highest microhardness). The microhardness decreases when the Sn concentration rises above 3.0 weight percent. For longer aging times (64 and 128 h), the microhardness increased continuously as the Sn content increased up to 3 wt.%. For instance, after aging for 128h, the microhardness of Sn-containing alloys (0.5, 1.5, and

3.0 wt.%) increased by 5.2%, 14.3%, and 25.3%, respectively, when compared to the ZC binary alloy. The microhardness of the Sn-containing alloys (3.5 and 4.0 wt.% Sn) declined and remained nearly the same after 128 h of aging.

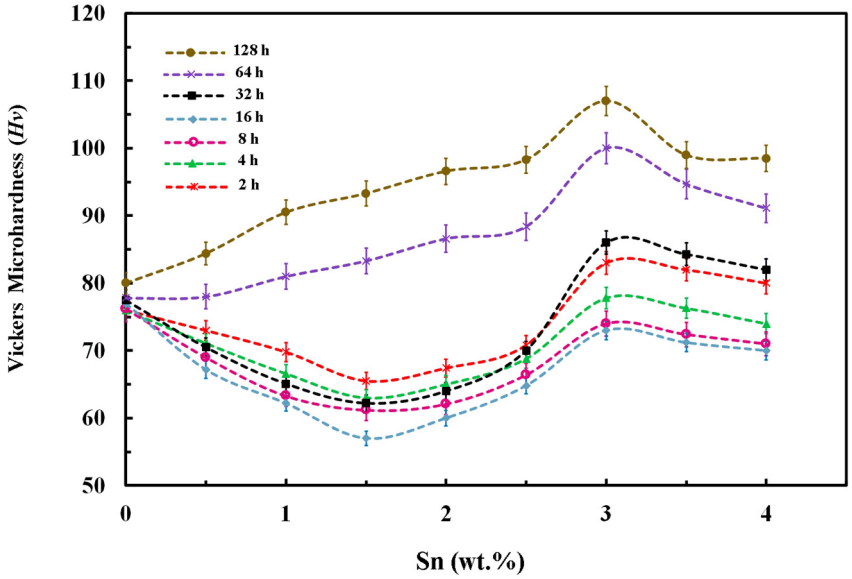


Figure 6. Effect of Sn content on the microhardness of Zn-4Cu-Sn alloys aged at 100 °C for various times.

The essential factors affecting precipitation-hardenable alloys' characteristics are the morphology, distribution, and volume fraction of the new second-phase precipitates in the matrix [34,35]. Representative SEM images of the ZC-0.5Sn and ZC-1.5Sn samples aged for 2 h are shown, respectively, in Figure 7a,b. Notably, the ternary alloys' microstructure consists of the primary α-Zn and ε-$CuZn_5$ phases and newly networked microstructures with different morphologies formed due to the Sn addition. The networked microstructures were identified as a $Cu_{81}Sn_{22}$ phase. These microstructures are comparable to those earlier described in the literature by Liu et al. [36]. The quantitative analysis with EDS results was used to evaluate the composition of the $Cu_{81}Sn_{22}$ phase. Figure 7c depicts that the $Cu_{81}Sn_{22}$ phase is composed of 74.30 wt.% Cu, 20.35 wt.% Sn, and 5.35 wt.% Zn. It was reported [37] that the Sn-Zn binary phase diagram is of the simple eutectic type. At 198.5 °C and the content of 85.1 at.% Sn, the eutectic reaction L → α-Zn + β-Sn proceeds. The Zn limit solubility in Sn is about 0.6 at.% Zn at this temperature, while the maximum solubility of Sn in hexagonal Zn is approximately 0.039 at.% Sn (extremely small). Because of the limited solubility of Sn in the α-Zn matrix and its high ductility, Sn tends to react with Cu to develop new IMCs. Using energy dispersive spectroscopy, the $Cu_{81}Sn_{22}$ phase was determined to be present in the IMC precipitates (Figure 7c). Similar trends were also detected by Sharma et al. [38], who observed the development of the $Cu_{81}Sn_{22}$ phase when the concentration of Sn exceeded 0.05%. Identical microstructures can be seen when comparing the micrographs presented in Figure 7, but the volume fraction of the $Cu_{81}Sn_{22}$ IMCs varies. ZC-1.5Sn alloy has a higher volume fraction of $Cu_{81}Sn_{22}$ precipitates than those for the ZC-0.5Sn alloy. However, with the addition of 0.5, 1.0, and 1.5wt%. Sn to the ZC alloy, the volume fraction of the $Cu_{81}Sn_{22}$ IMCs increases, while the volume fraction of the primary α-Zn phase decreases. Meanwhile, the volume fraction of the $CuZn_5$ IMCs is almost constant. Due to the precipitation of the $Cu_{81}Sn_{22}$ phase, which is a brittle phase, the microhardness of the alloys will be reduced. These findings are consistent with the data previously reported by Takahashi et al. [39], who stated that the ε-$CuZn_5$ phase is coarsely crystallized in the liquid phase. Although the precipitation of the ε-$CuZn_5$ phase caused a hardening of Zn-4Cu alloys, the effect was minor when compared to the precipitation of the $Cu_{81}Sn_{22}$ phase.

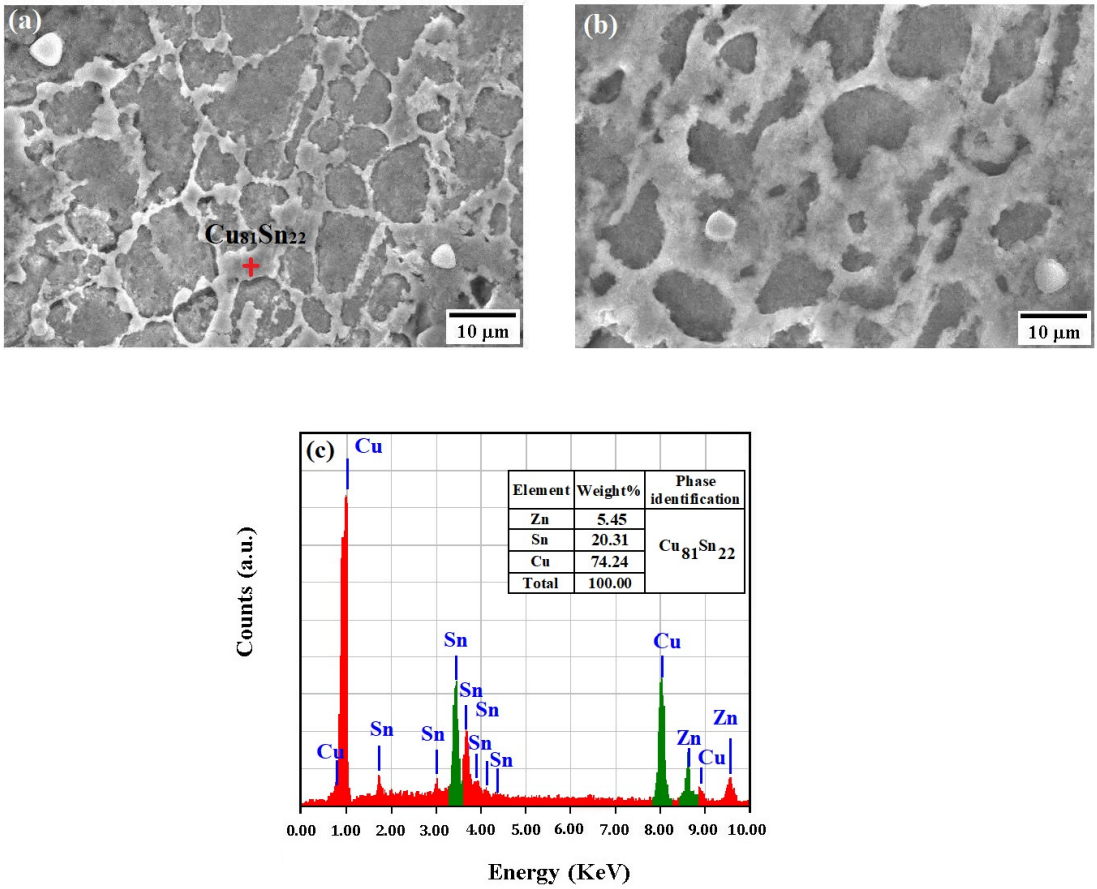


Figure 7. Representative SEM micrographs of (**a**) ZC-0.5Sn and (**b**) ZC-1.5Sn alloys aged at 100 °C for 2 h and (**c**) EDS results of $Cu_{81}Sn_{22}$ phase.

When the aging time is increased from 2 to 16 h, the microhardness of all Sn-containing alloys (0.5, 1.0, and 1.5 wt.%) decreases significantly when compared to samples aged for 2 h (Figure 6). Typical SEM micrographs of the ZC-0.5Sn and ZC-1.5Sn specimens aged for 16 h are displayed in Figure 8a,b, respectively. From Figures 7 and 8, one can conclude that the volume fraction of $Cu_{81}Sn_{22}$ IMCs in the 16 h aged samples is considerably greater than that of the 2 h aged samples, which could explain the higher microhardness values for samples aged for 16 h. When the aging duration reaches 32 h, the microhardness of all Sn-containing alloys (0.5, 1.0, and 1.5 wt.%) exhibited the same trend as samples aged for 16 h, but with higher values. The microstructure evolution of ZC-0.5Sn and ZC-1.5Sn samples aged for 32 h showed the development of new second-phase precipitates, as displayed in Figure 8a,b, respectively. EDS data confirmed that the new phase is a eutectic α-Zn + β-Sn structure composed of approximately 86.67 wt.% Sn, 12.40 wt.% Zn, and 0.93 Cu (see Figure 8c). The similarities between this microstructure and others previously reported in the literature are observed [40,41]. The formation of the eutectic α-Zn + β-Sn structure, along with the $CuZn_5$ and $Cu_{81}Sn_{22}$ phases, promoted precipitation hardening. Tian et al. [42] reported that the initiation and movement of dislocations, promoting the ductility enhancement, are hindered by internal obstacles such as solute atoms, grain boundaries, and second-phase particles to obtain high strength. Guo et al. [43] stated that when encountering pre-existing obstacles such as precipitates/matrix interfaces, dislocation loops undergo pile-up and result in hardening. The presence of a eutectic structure produces additional barriers for dislocation motion, leading to higher microhardness values compared to samples aged for 16 h. It should be observed that although the precipitation of the eutectic structure has a positive impact on microhardness, the impact is minimal compared to the existence of the $Cu_{81}Sn_{22}$ phase.

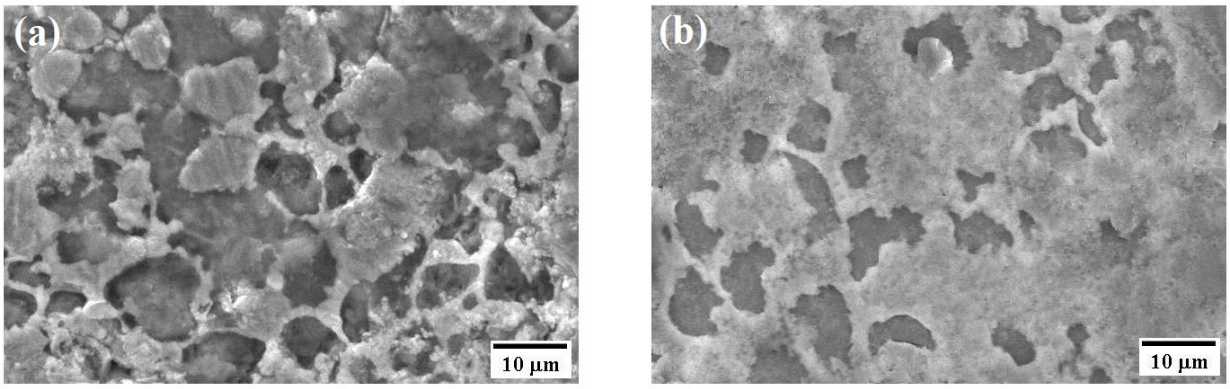


Figure 8. Representative SEM micrographs of (**a**) ZC-0.5Sn and (**b**) ZC-1.5Sn alloys aged at 100 °C for 16 h.

Referring to Figure 6, it can be perceived that the microhardness increased with an increasing Sn content from 1.5 to 3.0 wt.% at lower aging times (2 to 32 h). For instance, the microhardness of the ZC-3.0Sn sample increased by 27.6% compared to the ZC-1.5Sn sample after aging for 32 h. Figure 9a,b shows typical SEM images of the ZC-2.0Sn and ZC-3.0Sn samples aged for 32 h, respectively. It is interesting to notice that the microstructure consists of the primary α-Zn matrix, eutectic α-Zn + β-Sn structure, and γ-Cu_5Zn_8 phase. An EDS analysis was carried out to confirm the chemical composition of the γ-Cu_5Zn_8 phase, as shown in Figure 9c. However, the ε-$CuZn_5$ precipitates are not detected in all Sn-containing alloys (2.0, 2.5, and 3.0 wt.%). The reason may be that the addition of Sn promotes the formation of a eutectic α-Zn + β-Sn structure, which results in an increase in the atomic ratio of Cu to Zn, preferentially forming a γ-Cu_5Zn_8 phase rather than ε-$CuZn_5$ phase. Pstruś [44] stated that the ε-$CuZn_5$ phase exists only during the early stages of the aging process. The γ-Cu_5Zn_8 precipitates develop after some time, depending on the aging temperature and time of aging. The time required for its formation increases as the temperature decreases. It was reported [45,46] that the activation energy of the γ-$CuZn_5$ phase growth is much lower than that of the γ-Cu_5Zn_8 phase. Therefore, it could be expected that the first phase to form would be the ε-phase, which agrees with our work. The ε-phase transformed into the γ-phase because it is more thermodynamically stable. This is in line with the earlier work of Wei et al. [47], who concluded that the ε-phase was consumed by the formation of the γ-one during the aging process. When the Sn content increased from 2.0 to 3 wt.%, the volume fraction of the γ-Cu_5Zn_8 precipitates increased (see Figure 9), resulting in high reported microhardness values.

For the samples with higher levels of Sn concentration (3.5 and 4.0 wt.% Sn), the microhardness dropped. This trend may be explained by the presence of massive IMCs (γ-Cu_5Zn_8 precipitates and eutectic texture) within the matrix. These intermetallic compounds are brittle phases that, when subjected to a load, can easily cause stress concentration, which in turn can initiate and propagate microcracks in solder joints, leading to the failure of electronic components. The preceding interpretation based on the development of microcracks is strongly supported by SEM investigations. Figure 10a,b exhibits typical SEM images of the ZC-3.5Sn and ZC-4.0Sn samples aged for 32 h, respectively. Microcracks (locations denoted by arrows) may have been initiated during the microstructure's development. As the Sn content rose from 3.5 to 4.0 wt.%, the total crack length of the alloy grew.

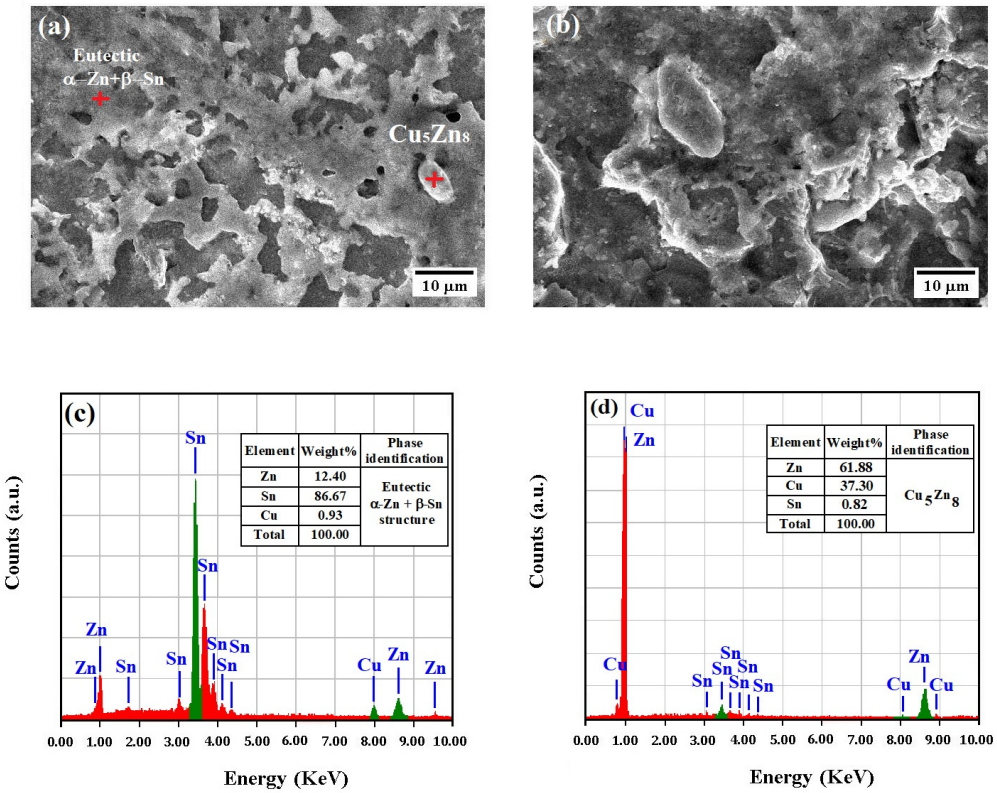


Figure 9. Representative SEM micrographs of (**a**) ZC-2.0Sn and (**b**) ZC-3.0Sn alloys aged at 100 °C for 32 h, (**c**) EDS results of eutectic α-Zn + β-Sn structure and (**d**) EDS results of γ-Cu_5Zn_8 phase.

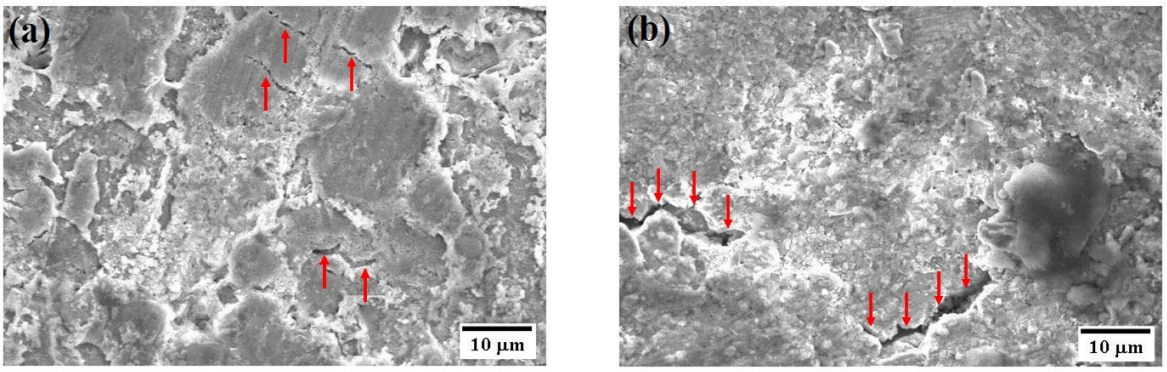


Figure 10. Representative SEM micrographs of (**a**) ZC-3.5Sn and (**b**) ZC-4.0Sn alloys aged at 100 °C for 32 h.

It should be noted that Cu_6Sn_5 and Cu_3Sn phases were not noticed in the present study. Our findings are consistent with those earlier documented by other scientists on various alloys [48–50]. The γ-Cu_5Zn_8 precipitates have a much lower Gibbs free energy formation (ΔG) than Cu_6Sn_5 and Cu_3Sn precipitates. The ΔG of the γ-Cu_5Zn_8 phase = −12.34 kJ/mol, which was much lower than that of the Cu_3Sn phase (ΔG = −7.78 kJ/mol) and Cu_6Sn_5 phase (ΔG = −7.42 kJ/mol). Consequently, the γ-Cu_5Zn_8 phase should form first [51,52]. Because Cu reacts more strongly with Zn than Sn, all the Cu was consumed in the development of Cu-Zn IMCs (ε-$CuZn_5$ and γ-Cu_5Zn_8). Consequently, the Cu_6Sn_5 and Cu_3Sn precipitates were not detected in the current work.

At high aging times (64 and 128 h), the microhardness of all Sn-containing samples increased continuously when increasing the Sn content from 0.0 to 3.0 wt.% (Figure 6). Adding Sn improved the age-hardening response. The optimal aging condition was reached at 3.0 wt.% Sn for all Sn-containing alloys. When the Sn-containing alloys (3.5

and 4.0 wt.% Sn) were aged for 64 and 128 h, the hardness declined by 7.94% and 8.90% compared to their peak aging hardness values, respectively. The impact of Sn addition on the age-hardening response profile of the current alloys can be inferred from their microstructures. Figure 11a,b demonstrates typical SEM images of ZC-1.5Sn samples aged for 64 and 128 h, respectively. Meanwhile, Figure 12a,b shows representative SEM micrographs for ZC-3.0Sn samples for 64 and 128 h, respectively. While the volume fraction of precipitates varies, the microstructure remains constant. The microstructure investigation showed the precipitation of the α-Zn +β-Sn eutectic structure and γ-Cu_5Zn_8 phase. The ε-$CuZn_5$ phase was not observed at high aging times (64 and 128 h). This observation may be elucidated due to the fact that when aging time increases, more Cu atoms diffuse towards the ε-$CuZn_5$ precipitates (formed during the solidification process), and the γ-Cu_5Zn_8 IMC develops. Additionally, the Sn inclusion enhances the development of the α-Zn + β-Sn eutectic structure, which increases the atomic ratio of Cu to Zn and favors the development of the γ-Cu_5Zn_8 precipitates rather than the ε-$CuZn_5$. This is in line with the earlier work of Wei et al. [46], who stated that the ε-$CuZn_5$ phase forms only in the initial stage of the aging process. When Figures 11 and 12 are compared, it is evident that the specimens aged for 128 h had a higher volume fraction of eutectic structure and γ-Cu_5Zn_8 IMCs than that of specimens aged for 64 h, which may account for the higher microhardness values for these samples.

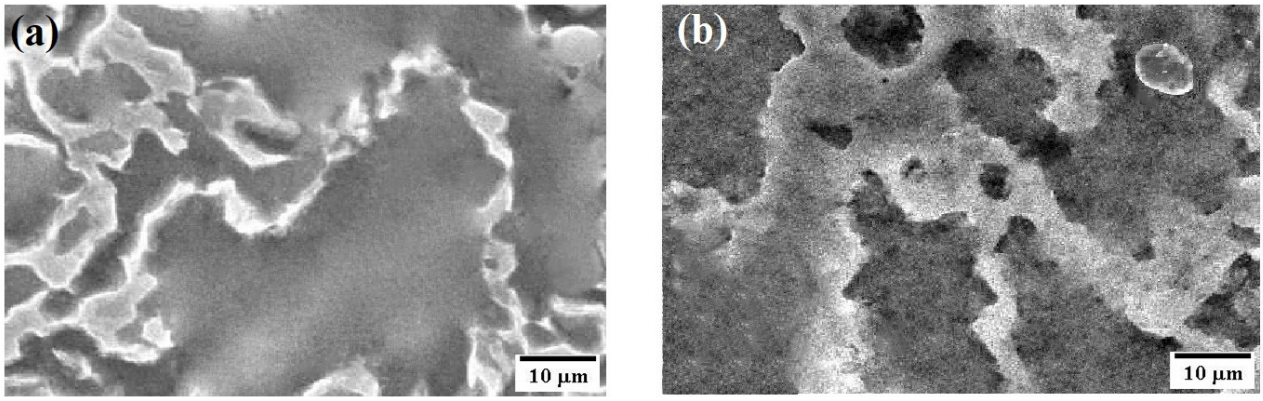


Figure 11. Representative SEM micrographs of ZC-1.5Sn samples aged at 100 °C for (**a**) 64 h and (**b**) 128 h.

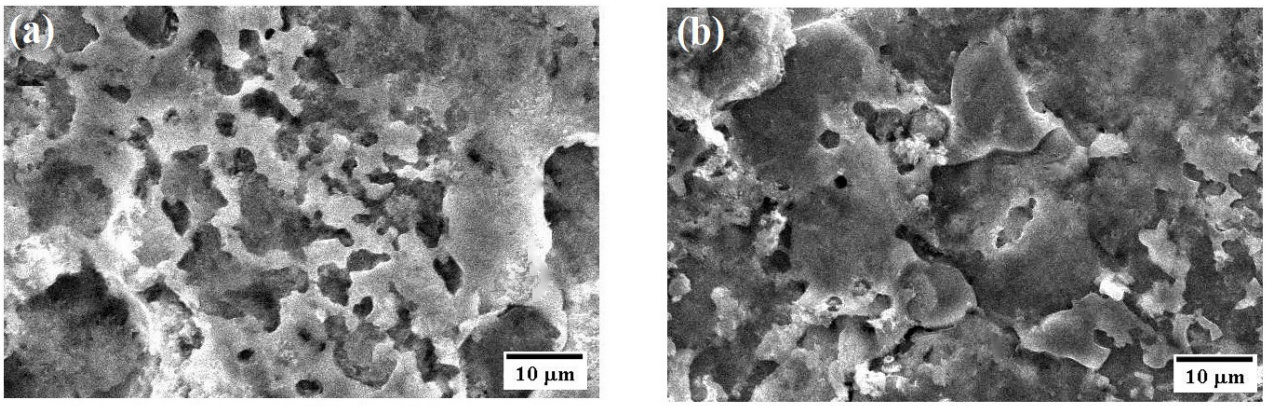


Figure 12. Representative SEM micrographs of ZC-3.0Sn samples aged at 100 °C for (**a**) 64 h and (**b**) 128 h.

In comparison to other alloys, the addition of 3.5 and 4.0 wt.% Sn has deleterious impacts on the microhardness. It is expected that the coarse eutectic structure and γ-Cu_5Zn_8 IMCs evolved in the matrix could lead to a reduction in microhardness. As previously

stated by some authors [53–55], the growth of thick and brittle IMCs may serve as favorable points for cracks, reducing the microhardness. This explanation agrees with the present results showing the decline in microhardness. Figure 13a,b demonstrates typical SEM images of ZC-4Sn samples aged for 64 and 128 h, respectively. Figure 8 confirms that the total crack length of the alloy increased as the Sn content increased from 3.5 to 4.0 wt.%, resulting in lower microhardness values (Figure 5).

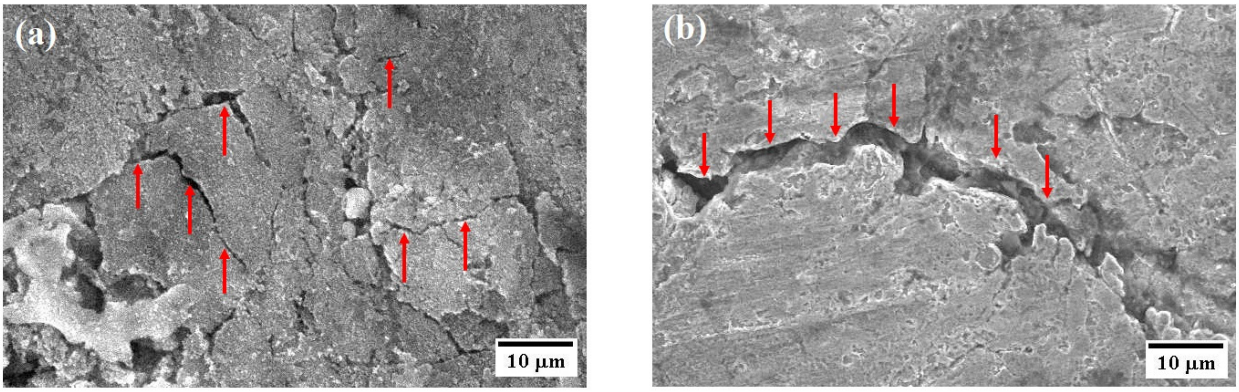


Figure 13. Representative SEM micrographs of ZC-4.0Sn samples aged at 100 °C for (**a**) 64 h and (**b**) 128 h.

The aforementioned discussion has been confirmed by further X-ray diffraction (XRD) measurements. XRD can offer precise information regarding the internal state of a material after the aging process. Figure 14 illustrates the XRD patterns for the ZC-1.5Sn alloy aged at 100 °C for different aging times (2 to 128 h) as a representative example. From XRD data and the analysis of the diffraction peaks, it was confirmed that three phases are observed for the aged alloy for (2 to 16 h). The diffraction peaks of α-Zn phase (JCPDS Card No. 01-087-0713), $Cu_{81}Sn_{22}$ (JCPDS Card No. 00-031-0486), and ε-$CuZn_5$ (JCPDS Card No. 00-035-1151) IMCs were observed at the low range aging time. For the sample aged for 32 h, the b-Sn diffraction peaks appeared with the tetragonal structure according to (JCPDS card No. 04-0673) due to the presence of eutectic α-Zn + β-Sn structure. At high aging times (64 and 128 h), the α-Zn + β-Sn eutectic structure and ε -Cu_5Zn_8 (JCPDS card No. 01-071-0397) peaks were detected. The $Cu_{81}Sn_{22}$ and ε-$CuZn_5$ diffraction peaks disappeared at high aging times (64 and 128 h). No presence of Cu_6Sn_5 and Cu_3Sn phases was detected in the XRD patterns of the studied alloys. With tin addition, it does not react with copper in the examined alloys, but Cu reacts with Zn and forms the Cu_5Zn_8 IMC. The reason rendered to the lower Gibbs free energy of γ-Cu_5Zn_8 formation ($\Delta G = -12.34$ kJ/mol) than that of η-Cu_6Sn_5 ($\Delta G = -7.42$ kJ/mol) [45]. As a result of the reaction, the amount of zinc in the solder alloy is greatly reduced [56]. Also, the formation of Cu_5Zn_8 IMC was confirmed by Xiao et al. [57]. This finding might explain that the γ-Cu_5Zn_8 IMC forms as more copper atoms diffuse towards the ε-$CuZn_5$ precipitate through the aging time increment. Furthermore, the tin addition promotes the growth of the α-Zn + β-Sn eutectic structure, which raises the atomic ratio of Cu to Zn and encourages the formation of the γ-Cu_5Zn_8 rather than the ε-$CuZn_5$ precipitates.

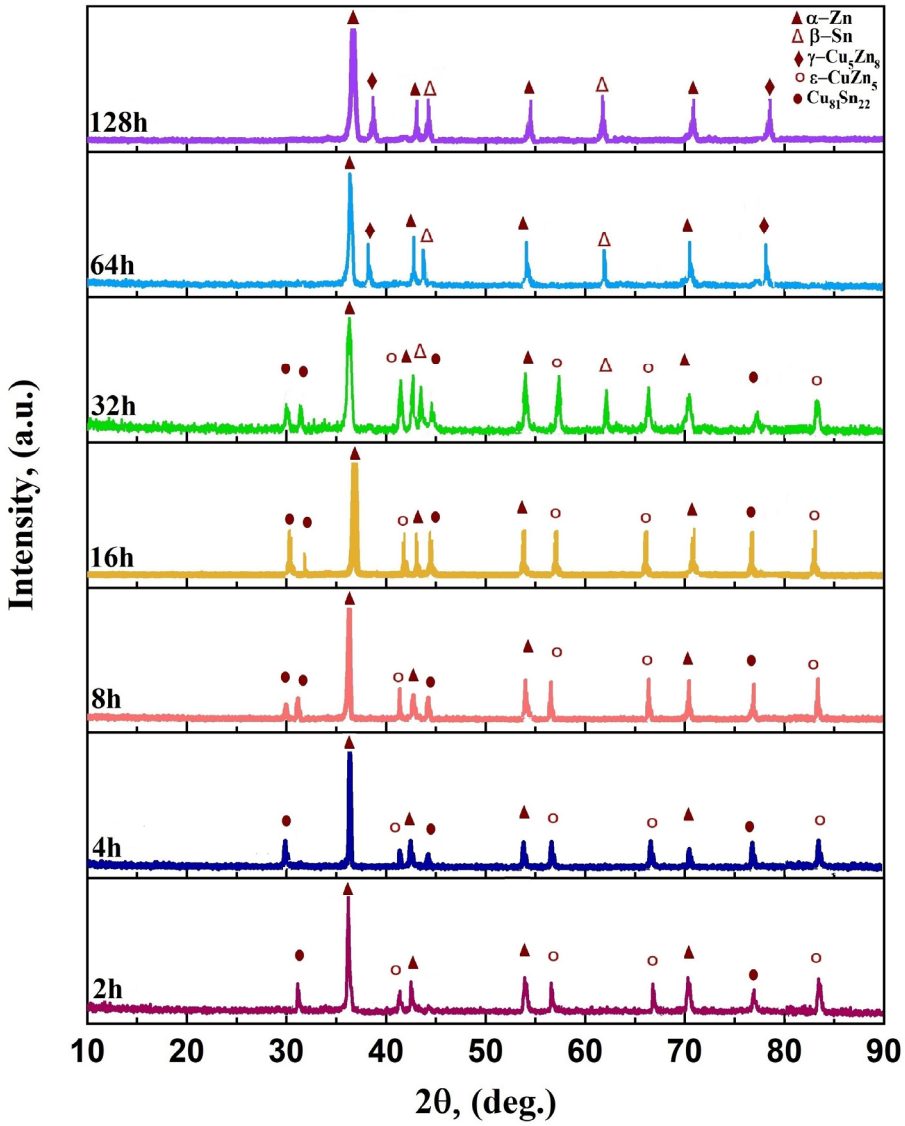


Figure 14. Representative XRD patterns of the ZC-1.5Sn alloy aged at 100 °C for different aging times.

The crystalline lattice parameters *a*, *c*, *c/a* ratio and the unit cell volume (*V*) were calculated for α-Zn matrix at the aging temperature (100 °C) with different aging times (2 to 128 h) for all tin weight percentages. The calculated values were indexed in Table 2 with the aid of X-ray data. For the α-Zn phase of the hcp crystal structure, the interplanar distance, *d*, between these two planes (110) and (002) can be correlated to *a* and *c* lattice parameters through the following equation:

$$\frac{1}{d} = \frac{4}{3}\left(\frac{h^2 + hk + k^2}{a^2}\right) + \frac{l^2}{c^2} \quad (1)$$

Figure 15a illustrates the variation in *a* with aging time for all the investigated alloys aged at 100 °C. It is seen that the trend of the lattice parameter, *a*, was contrary to the behavior of the *c* parameter and the *c/a* ratio (Figure 15b,c) for the investigated alloys. For the ZC-0Sn alloy, their values remained roughly constant as the aging time changed. Figure 15a illustrates that the crystalline lattice parameter, *a*, decreased with aging time up to 16 h and then increased at high aging times (32–128 h). The lowest value of *a* was 2.6054 Å (for 1.5 wt.% Sn at 16 h), and it reached 2.7716 Å at the maximum aging time (128 h) for 3wt.%Sn. Figure 15b shows the lattice parameter's (*c*) dependence on aging time

at different Sn ratios. This figure shows that parameter *c* had the highest value of about 4.9504 Å (for 1.5 wt.% Sn at 16 h) and the lowest (4.8901 for 3wt.%Sn at 128 h). The aging time and Sn concentration had the same effect on the lattice parameter *c*, as did the *c/a* ratio. In the case of the α-Zn phase, the calculated values of *a* and *c* parameters agreed with the values recorded in (JCPDS Card No. 01-087-0713) and those shown in the literature [58]. The detected lattice parameters and the precipitation mechanism explored by XRD results inferred the microhardness behavior and the age-hardening response of the current alloys with the Sn addition.

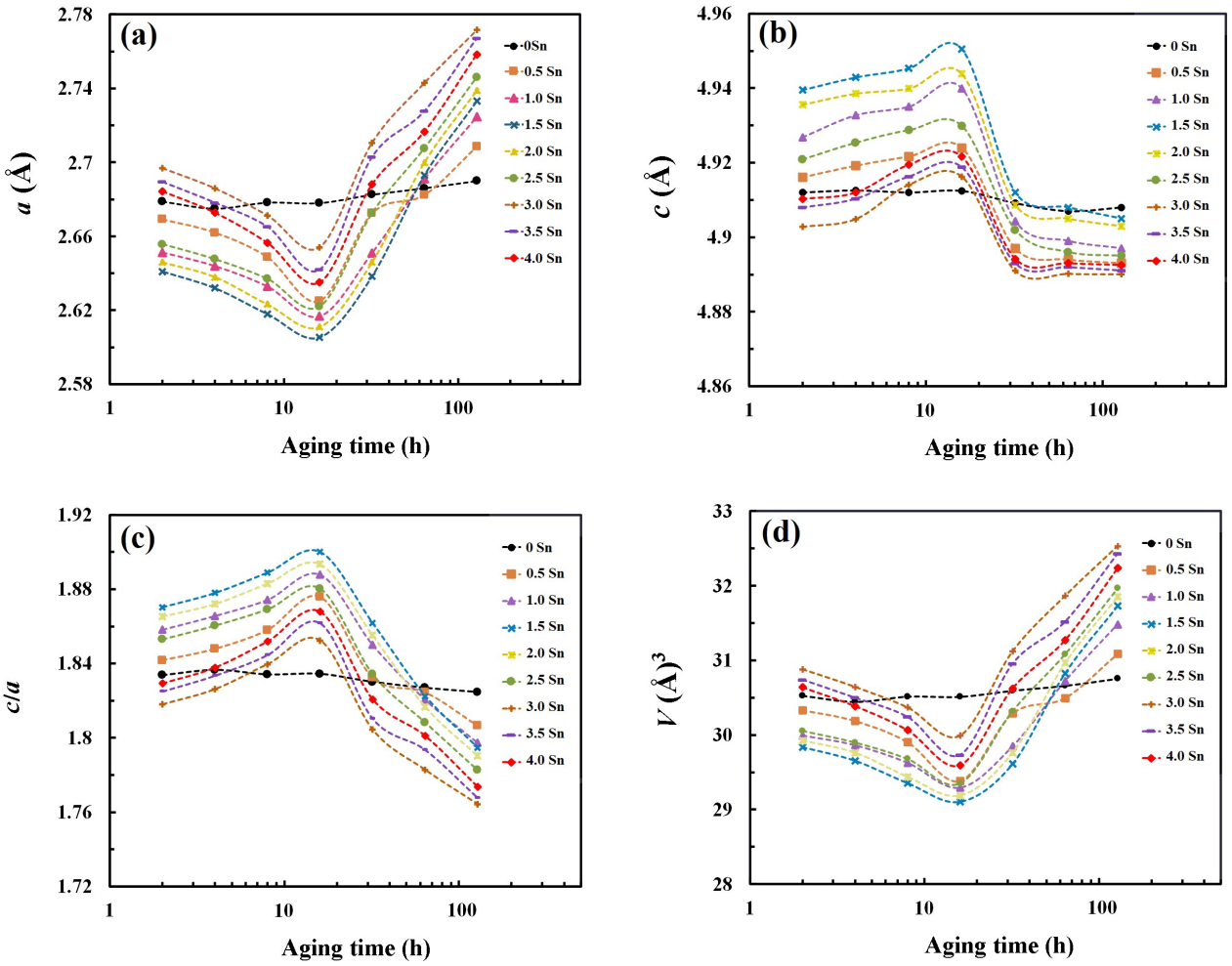


Figure 15. The variation in (**a**) the lattice parameter *a*, (**b**) the lattice parameter *c*, (**c**) the *c/a* ratio, and (**d**) the unit cell volume *V* for the α-Zn matrix with the aging time for all the investigated samples aged at 100 °C.

Table 2. The calculated crystalline lattice parameters *a*, *c*, *c/a* ratio and the unit cell volume *V* for the α-Zn matrix at different aging times and various Sn concentrations.

Lattice Parameter	Aging Time (h)	0 Sn wt.%	0.5 Sn wt.%	1.0 Sn wt.%	1.5 Sn wt.%	2.0 Sn wt.%	2.5 Sn wt.%	3.0 Sn wt.%	3.5 Sn wt.%	4.0 Sn wt.%
***a* (Å)**	**2**	2.6787	2.6692	2.6513	2.641	2.646	2.6557	2.6968	2.6893	2.6842
	4	2.675	2.662	2.644	2.632	2.638	2.6475	2.6859	2.6781	2.6727
	8	2.6782	2.6488	2.633	2.6180	2.6233	2.637	2.6713	2.6652	2.6564
	16	2.678	2.625	2.6168	2.6054	2.611	2.622	2.654	2.642	2.635
	32	2.6825	2.6724	2.651	2.6383	2.646	2.6724	2.7105	2.7028	2.688
	64	2.686	2.6824	2.691	2.693	2.6999	2.7076	2.743	2.7276	2.7166
	128	2.6899	2.7085	2.7246	2.733	2.7388	2.746	2.7716	2.767	2.7583

Table 2. *Cont.*

Lattice Parameter	Aging Time (h)	0 Sn wt.%	0.5 Sn wt.%	1.0 Sn wt.%	1.5 Sn wt.%	2.0 Sn wt.%	2.5 Sn wt.%	3.0 Sn wt.%	3.5 Sn wt.%	4.0 Sn wt.%
c (Å)	**2**	4.912	4.9161	4.9268	4.9395	4.9356	4.9209	4.9028	4.908	4.9102
	4	4.9125	4.9192	4.9327	4.9429	4.9385	4.9254	4.9048	4.9103	4.912
	8	4.9119	4.9217	4.935	4.9453	4.9399	4.9287	4.9141	4.9163	4.9194
	16	4.9124	4.924	4.9399	4.9504	4.9438	4.9299	4.9162	4.9188	4.9215
	32	4.9091	4.897	4.9043	4.912	4.9087	4.902	4.891	4.893	4.8942
	64	4.907	4.894	4.899	4.908	4.905	4.896	4.8902	4.892	4.8930
	128	4.908	4.893	4.897	4.905	4.903	4.895	4.8901	4.8911	4.8925
c/*a*	**2**	1.8336	1.8417	1.8582	1.8703	1.8653	1.8529	1.8180	1.8249	1.8293
	4	1.8364	1.8479	1.8656	1.8780	1.8720	1.8603	1.8261	1.8335	1.8378
	8	1.8340	1.8580	1.8742	1.8889	1.8830	1.8690	1.8395	1.8446	1.8518
	16	1.8343	1.8758	1.8877	1.9000	1.8934	1.8802	1.8523	1.8617	1.8677
	32	1.8300	1.8324	1.8499	1.8618	1.8551	1.8342	1.8044	1.8103	1.8207
	64	1.8268	1.8244	1.8205	1.8225	1.8167	1.8082	1.7827	1.7935	1.8011
	128	1.8246	1.8065	1.7973	1.7947	1.7902	1.7825	1.7643	1.7676	1.7737
$V = 0.866a^2c$	**2**	30.524	30.331	29.993	29.835	29.925	30.055	30.878	30.740	30.637
	4	30.441	30.187	29.862	29.653	29.762	29.899	30.642	30.499	30.386
	8	30.511	29.904	29.628	29.353	29.439	29.680	30.367	30.242	30.063
	16	30.509	29.382	29.293	29.101	29.187	29.350	29.988	29.733	29.592
	32	30.591	30.286	29.847	29.609	29.762	30.318	31.119	30.954	30.623
	64	30.658	30.495	30.722	30.824	30.963	31.083	31.86	31.518	31.271
	128	30.753	31.084	31.481	31.727	31.849	31.964	32.53	32.429	32.235

4. Conclusions

1. The microhardness of the Zn-4Cu (ZC) binary alloy increases slightly from 76 to 80 HV as the aging time increases from 2 to 128 h, respectively;
2. All Sn-containing alloys first exhibit a decrease in microhardness with increasing aging time up to 16 h, but the trend is then reversed;
3. The lowest hardness belongs to the ZC-1.5Sn alloy and the highest to ZC-3.0 alloy, with the remaining alloys lying in between;
4. The variations in the age-hardening response with increasing aging time and Sn content were determined based on the structural transformations that take place in the alloys;
5. The behavior of the lattice parameters, *a*, *c*, and the *c/a* ratio, as well as the unit cell volume *V* for the α-Zn matrix, with the aging time for all the investigated alloys, is compatible with the trend of microhardness behavior.

Author Contributions: Conceptualization, A.F.A.E.-R. and H.Y.Z.; investigation, A.F.A.E.-R., H.Y.Z. and A.E.S.; methodology, A.F.A.E.-R., H.Y.Z. and A.E.S.; writing—original draft, A.F.A.E.-R.; writing—review and editing, A.F.A.E.-R., H.Y.Z. and A.E.S. All authors have read and agreed to the published version of the manuscript.

Funding: This research was funded by the Deanship of Scientific Research at King Khalid University through the large group Research Project under grant number RGP2/325/44.

Data Availability Statement: The data presented in this study are available on request from the corresponding author. The data are not publicly available due to privacy.

Conflicts of Interest: The authors declare no conflict of interest.

References

1. Ramirez-Ledesma, A.L.; Roncagliolo-Barrera, P.; Alvarez-Perez, M.A.; Juarez-Islas, J.A.; Paternoster, C.; Copes, F.; Mantovani, D. Introducing novel bioabsorbable Zn–Ag–Mg alloys intended for cardiovascular applications. *Mater. Today Commun.* **2023**, *35*, 105544. [CrossRef]

2. Mollaei, N.; Razavi, S.H.; Aboutalebi, M.R.; Fatemi, S.M. Effect of Mn addition on the microstructure, mechanical, and corrosion properties of an extruded biodegradable Zn–0.2Mg alloy. *J. Mater. Sci. Technol.* **2023**, *22*, 1983–1998. [CrossRef]
3. Li, S.; Wang, X.; Ren, J.; Liu, C.; Hu, Y.; Yang, Y. Microstructure, mechanical property and corrosion behavior of biomedical Zn–Fe alloy prepared by low-temperature sintering. *J. Alloys Compd.* **2023**, *934*, 167812. [CrossRef]
4. An, F.; Ma, Z.; Sun, K.; Zhang, L.; Joo, S.; Ning, J.; Yu, H. Influences of the Ag content on microstructures and properties of Zne3MgexAg alloy by spark plasma sintering. *J. Mater. Sci. Technol.* **2023**, *24*, 595–607.
5. Li, H.F.; Xie, X.H.; Zheng, Y.F.; Cong, Y.; Zhou, F.Y.; Qiu, K.J.; Wang, X.; Chen, S.H.; Huang, L.; Tian, L.; et al. Development of biodegradable Zn-1X binary alloys with nutrient alloying elements Mg, Ca and Sr. *Sci. Rep.* **2015**, *5*, 10719. [CrossRef]
6. Gong, H.; Wang, K.; Strich, R.; Zhou, J.G. In vitro biodegradation behavior, mechanical properties, and cytotoxicity of biodegradable Zn–Mg alloy. *J. Biomed. Mater. Res. Part B Appl. Biomater.* **2015**, *103*, 1632–1640. [CrossRef]
7. Kafri, A.; Ovadia, S.; Yosafovichdoitch, G.; Aghion, E. In vivo performances of pure Zn and Zn–Fe alloy as biodegradable implants. *J. Mater. Sci. Mater. Med.* **2018**, *29*, 94. [CrossRef] [PubMed]
8. Li, P.; Schille, C.; Schweizer, E.; Rupp, F.; Heiss, A.; Legner, C.; Scheideler, L. Mechanical characteristics, in vitro degradation, cytotoxicity, and antibacterial evaluation of Zn–4.0Ag alloy as a biodegradable material. *Int. J. Mol. Sci.* **2018**, *19*, 755. [CrossRef]
9. Zou, Y.L.; Chen, X.; Chen, B. Effects of Ca concentration on degradation behavior of Zn–x Ca alloys in Hanks' solution. *Mater. Lett.* **2018**, *218*, 193–196. [CrossRef]
10. Shi, Z.Z.; Yu, J.; Liu, X.F. Microalloyed Zn–Mn alloys: From extremely brittle to extraordinarily ductile at room temperature. *Mater. Des.* **2018**, *144*, 343–352. [CrossRef]
11. Xiao, L.R.; Zhang, X.M.; Wang, Y.; Li, W.; Sun, Q.S.; Geng, Z.J. High temperature creep behavior of Zn-1.0Cu-0.2Ti alloy. *Adv. Mater. Res.* **2011**, *287*, 769–776. [CrossRef]
12. Wang, K.; Tong, X.; Lin, J.X.; Wei, A.P.; Li, Y.C.; Dargusch, M.; Wen, C.E. Binary Zn–Ti alloys for orthopedic applications: Corrosion and degradation behaviors, friction and wear performance, and cytotoxicity. *J. Mater. Sci. Technol.* **2021**, *74*, 216–229. [CrossRef]
13. Zhao, S.; Seitz, J.M.; Eifler, R.; Maier, H.J.; Guillory, R.J., II; Earley, E.J.; Drelich, A.; Goldman, J.; Drelich, J.W. Zn–Li alloy after extrusion and drawing: Structural, mechanical characterization, and biodegradation in abdominal aorta of rat. *Mater. Sci. Eng. C* **2017**, *76*, 301–312. [CrossRef]
14. Tong, X.; Zhang, D.C.; Lin, J.X.; Dai, Y.L.; Luan, Y.N.; Sun, Q.X.; Shi, Z.M.; Wang, K.; Gao, Y.; Lin, J.G.; et al. Development of biodegradable Zn–1Mg–0.1RE (RE = Er, Dy, and Ho) alloys for biomedical applications. *Acta Biomater.* **2020**, *117*, 384–399. [CrossRef]
15. Chen, Q.; Thouas, G.A. Metallic implant biomaterials. *Mater. Sci. Eng. R.* **2015**, *87*, 1–57. [CrossRef]
16. Tang, Z.; Huang, H.; Niu, J.; Zhang, L.; Zhang, H.; Pei, J.; Tan, J.; Yuan, G. Design and characterizations of novel biodegradable Zn-Cu-Mg alloys for potential biodegradable implants. *Mater. Des.* **2017**, *117*, 84–94. [CrossRef]
17. Huang, S.; Liu, H.; Su, Y.; Qiao, L.; Yan, Y. Significant influence of trace Li on the mechanical properties, corrosion behavior, and antibacterial properties of biodegradable Zn–4Cu alloys. *J. Mater. Sci. Technol.* **2023**, *151*, 245–257. [CrossRef]
18. Mostaed, E.; Ardakani, M.S.; Sikora-Jasinska, M.; Drelich, J.W. Precipitation induced room temperature superplasticity in Zn-Cu alloys. *Mater. Lett.* **2019**, *244*, 203–206. [CrossRef]
19. Huang, J.; Lai, Y.; Jin, H.; Guo, H.; Ai, F.; Xing, Q.; Yang, X.; Ross, D.J. Preparation and properties of Zn-Cu alloy for potential stent material. *J. Mater. Eng. Perform.* **2020**, *29*, 6484–6493. [CrossRef]
20. Yue, R.; Huang, H.; Ke, G.; Zhang, H.; Pei, J.; Xue, G.; Yuan, G. Microstructure, mechanical properties and in vitro degradation behavior of novel Zn-Cu-Fe alloys. *Mater. Char.* **2017**, *134*, 114–122. [CrossRef]
21. Tang, Z.; Niu, J.; Huang, H.; Zhang, H.; Pei, J.; Ou, J.; Yuan, G. Potential biodegradable Zn-Cu binary alloys developed for cardiovascular implant applications. *J. Mech. Behav. Biomed. Mater.* **2017**, *72*, 182–191. [CrossRef] [PubMed]
22. Niu, J.; Tang, Z.; Huang, H.; Pei, J.; Zhang, H.; Yuan, G.; Ding, W. Research on a Zn-Cu alloy as a biodegradable material for potential vascular stents application. *Mater. Sci. Eng. C* **2016**, *69*, 407–413. [CrossRef]
23. Qian, Y.; Yuan, G.Y. Research status, challenges, and countermeasures of biodegradable zinc-based vascular stents. *Acta Metall. Sin.* **2021**, *57*, 272–282.
24. Mostaed, E.; Sikora-Jasinska, M.; Drelich, M.; Vedani, J.W. Zinc-based alloys for degradable vascular stent applications. *Acta Biomater.* **2018**, *71*, 1–23. [CrossRef]
25. Abou El-Khair, M.T.; Daoud, A.; Ismail, A. Effect of different Al contents on the microstructure, tensile and wear properties of Zn-based alloy. *Mater. Lett.* **2004**, *58*, 1754–1760. [CrossRef]
26. Porter, F. *Zinc Handbook: Properties, Processing, and Use in Design*; CRC Press: New York, NY, USA, 1991.
27. Liu, H.; Ye, L.; Ren, K.; Sun, C.; Zhuo, X.; Yan, K.; Ju, J.; Jiang, J.; Xue, F.; Bai, J. Evolutions of $CuZn_5$ and Mg_2Zn_{11} phases during ECAP and their impact on mechanical properties of Zn-Cu-Mg alloys. *J. Mater. Sci. Technol.* **2022**, *21*, 5032–5044. [CrossRef]
28. Zhang, L.; Liu, X.Y.; Huang, H.; Zhan, W. Effects of Ti on microstructure, mechanical properties and biodegradation behavior of Zn-Cu alloy. *Mater. Lett.* **2022**, *244*, 119–122. [CrossRef]
29. Lin, J.; Tong, X.; Wang, K.; Shi, Z.; Li, Y.; Dargusch, M.; Wen, C. Biodegradable Zn–3Cu and Zn–3Cu–0.2Ti alloys with ultrahigh ductility and antibacterial ability for orthopedic applications. *J. Mater. Sci. Technol.* **2021**, *68*, 76–90. [CrossRef]
30. Wang, H.; Zhang, Y.; Wang, C.; Cao, S.; Bai, W.; Wu, C.; Qian, J. Effect of Al content on microstructure and properties of Zn–Cu–Al alloy. *IOP Conf. Ser. Mater. Sci. Eng.* **2019**, *746*, 012018. [CrossRef]

31. Su, Y.; Lin, X.; Meng, W.; Huang, W. Phase and microstructure pattern selection of Zn-rich Zn–Cu peritectic alloys during laser surface remelting. *J. Mater. Sci.* **2021**, *56*, 14314–14332. [CrossRef]
32. Kejzlar, P.; Machuta, J.; Nová, I. Comparison of the structure of CuZn40MnAl alloy casted into sand and metal moulds. *Manuf. Technol.* **2017**, *17*, 44–48. [CrossRef]
33. Kattner, U.; Massalski, T.B. *Binary Alloy Phase Diagrams*; ASM International: Material Park, OH, USA, 1990; p. 148.
34. Abdelaziz, S.M.; Lebda, H.I.; Abd El-Rehim, A.F.; Habashy, D.M. Modeling and experimental investigation of indentation creep behavior of hypoeutectic Sn–Bi and Sn–Bi–Sb_2O_3 alloys using genetic programming approach. *Phys. Scr.* **2023**, *98*, 065912. [CrossRef]
35. Abd El-Rehim, A.F.; Habashy, D.M.; Zahran, H.Y.; Soliman, H.N. Mathematical modelling of vickers hardness of Sn–9Zn–Cu solder alloys using an artificial neural network. *Met. Mater. Int.* **2021**, *27*, 4084–4096. [CrossRef]
36. Liu, L.; Zhu, J.B.; Zhang, C.; Li, J.C.; Jiang, Q. Microstructure and the properties of $FeCoCuNiSn_x$ high entropy alloys. *Mater. Sci. Eng. A* **2012**, *548*, 64–68. [CrossRef]
37. Hu, J.; Yin, F.; Zhao, M.; Ouyang, X. Experimental investigation and thermodynamic calculation of the Co–Sn–Zn ternary system. *J. Alloys Compds.* **2018**, *747*, 815–825. [CrossRef]
38. Sharma, A.; Lee, H.; Ahn, B. Tailoring compressive strength and absorption energy of lightweight multi-phase AlCuSiFeX (X = Cr, Mn, Zn, Sn) high-entropy alloys processed via powder metallurgy. *Materials* **2021**, *14*, 4945. [CrossRef]
39. Takahashi, T.; Komatsu, S.; Nishikawa, H.; Takemoto, T. Improvement of high-temperature performance of Zn–Sn solder joint. *J. Electron. Mater.* **2010**, *39*, 1241–1247. [CrossRef]
40. Li, Q.; Chan, Y.C.; Zhang, K.; Yung, K.C. Study of microstructure evolution in novel Sn–Zn/Cu bi-layer and Cu/Sn–Zn/Cu sandwich structures with nanoscale thickness for 3D packaging interconnection. *Microelectron. Eng.* **2014**, *122*, 52–58. [CrossRef]
41. Mahmudi, R.; Eslami, M. Impression creep behavior of Zn–Sn high-temperature lead-free solders. *J. Electron. Mater.* **2010**, *39*, 2495–2502. [CrossRef]
42. Tian, X.; Zhao, Y.; Gu, T.; Guo, Y.; Xu, F.; Hou, H. Cooperative effect of strength and ductility processed by thermomechanical treatment for Cu–Al–Ni alloy. *Mat. Sci. Eng. A* **2022**, *849*, 143485. [CrossRef]
43. Guo, Q.; Hou, H.; Pan, Y.; Pei, X.; Song, Z.; Liaw, P.K.; Zhao, Y. Hardening-softening of $Al_{0.3}$CoCrFeNi high-entropy alloy under nanoindentation. *Mater. Des.* **2023**, *231*, 112050. [CrossRef]
44. Pstruś, J. Early stages of wetting of copper by Sn–Zn eutectic alloy. *J. Mater. Sci. Mater. Electron.* **2018**, *29*, 20531–20545. [CrossRef]
45. Lee, C.S.; Shieu, F.S. Growth of intermetallic compounds in the Sn–9Zn/Cu joint. *J. Electron. Mater.* **2006**, *35*, 1660–1664. [CrossRef]
46. Mayappan, R.; Ahmad, Z.A. Effect of Bi addition on the activation energy for the growth of Cu_5Zn_8 intermetallic in the Sn–Zn lead-free solder. *Intermetallics* **2010**, *18*, 730–735. [CrossRef]
47. Wei, Y.; Liu, Y.; Zhao, X.; Tan, C.; Dong, Y.; Zhang, J. Effects of minor alloying with Ge and in on the interfacial microstructure between Zn–Sn solder alloy and Cu substrate. *J. Alloys Compds.* **2020**, *831*, 154812. [CrossRef]
48. Shen, J.; Pu, Y.; Yin, H.; Luo, D.; Chen, J. Effects of minor Cu and Zn additions on the thermal, microstructure and tensile properties of Sn–Bi-based solder alloys. *J. Alloys Compds.* **2014**, *614*, 63–70. [CrossRef]
49. Hamada, N.; Uesugi, T.; Takigawa, Y.; Higashi, K. Effect of addition of small amount of zinc on microstructural evolution and thermal shock behavior in low-Ag Sn–Ag–Cu solder joints during thermal cycling. *Mater. Trans.* **2013**, *54*, 796–805. [CrossRef]
50. Li, J.F.; Mannan, S.H.; Clode, M.P.; Whalley, D.C.; Hutt, D.A. Interfacial reactions between molten Sn–Bi–X solders and cu substrates for liquid solder interconnects. *Acta Mater.* **2006**, *54*, 2907–2922. [CrossRef]
51. Zahran, H.Y.; Soliman, H.N.; Abd El-Rehim, A.F.; Habashy, D.M. Modelling the effect of Cu content on the microstructure and Vickers microhardness of Sn-9Zn binary eutectic alloy using an artificial neural network. *Crystals* **2021**, *11*, 481. [CrossRef]
52. Islam, M.N.; Chan, Y.C.; Rizvi, M.J.; Jillek, W. Investigations of interfacial reactions of Sn–Zn based and Sn–Ag–Cu lead-free solder alloys as replacement for Sn–Pb solder. *J. Alloys Compds.* **2005**, *400*, 136–144. [CrossRef]
53. Silva, B.L.; Spinelli, J.E. Correlations of microstructure and mechanical properties of the ternary Sn-9wt% Zn-2wt% Cu solder alloy. *Mater. Res.* **2018**, *21*, e20170877. [CrossRef]
54. Zahran, H.Y.; Abd El-Rehim, A.F.; Alfaify, S. Effect of graphitic carbon nitride nanosheets addition on the microstructure and mechanical properties of Sn–3.5Ag–0.5Cu solder alloy. *J. Electron. Mater.* **2018**, *47*, 5614–5624. [CrossRef]
55. El-Daly, A.A.; Hammad, A.E. Effects of small addition of Ag and/or Cu on the microstructure and properties of Sn–9Zn lead-free solders. *Mater. Sci. Eng. A* **2010**, *527*, 5212–5219. [CrossRef]
56. Liu, H.; Wei, Y.; Zhang, Y.; Hou, Z.; Zhao, X. Effects of Bi and Cu addition on mechanical properties of Sn9Zn alloy and interfacial intermetallic growth with Ni substrate. *Mater. Today Commun.* **2023**, *35*, 106350. [CrossRef]
57. Xiao, J.; Tong, X.; Liang, J.; Chen, Q.; Tang, Q. Microstructure and morphology of the soldering interface of Sn–2.0Ag–1.5Zn low Ag content lead-free solder ball and different substrates. *Heliyon* **2023**, *9*, e12952. [CrossRef] [PubMed]
58. Narkevičius, A.; Bučinskienė, D.; Ručinskienė, A.; Pakštas, V.; Bikulčius, G. Study on long term atmospheric corrosion of electrodeposited zinc and zinc alloys. *Int. J. Surf. Sci. Eng. Coat.* **2013**, *91*, 68–73. [CrossRef]

Disclaimer/Publisher's Note: The statements, opinions and data contained in all publications are solely those of the individual author(s) and contributor(s) and not of MDPI and/or the editor(s). MDPI and/or the editor(s) disclaim responsibility for any injury to people or property resulting from any ideas, methods, instructions or products referred to in the content.